Exploring 60 GHz Millimeter-wave Indoor Propagation Path Loss Models and Capacity Enhancement for Modified Indoor Environments

Nidal Qasem

Department of Communications and Computer Engineering, Al-Ahliyya Amman University, Amman, Jordan
Email: ne.qasem@ammanu.edu.jo (N.Q.)

***Abstract*—Short-range communication systems have chosen the 60 GHz spectrum to fulfill consumers' demands for high data speeds. This frequency, nevertheless, is diminished by obstructions. This work aims to overcome the constraints of the 60 GHz band by enhancing interior surroundings through the implementation of Square Loop (SL) Frequency Selective Surfaces (FSSs) wallpaper, consequently maximizing its efficiency. Analyzed utilizing both MATLAB and CST Studio Suite tools, the response of the SL FSS wallpaper at a frequency of 61.5 GHz has been examined. The software 'Wireless InSite' is also utilized to showcase the improved transmission of waves within a building that has been altered with SL FSSs wallpaper. The demonstration is conducted on single input single output and multiple input multiple output systems to validate the efficacy of FSSs in enhancing the capacity of such systems, as well as to assess the impact of the human body on capacity. The simulation findings demonstrate that the use of SL FSS wallpaper to remodel a structure is an appealing approach to greatly enhancing the interior 60 GHz wireless communications band. This research additionally introduces and contrasts two extensive indoor propagation route loss models: the Close-In (CI) free space reference distance model and the floating intercept (FI) model. Analyzed data is derived from 'Wireless InSite' at distances ranging from 4 to 14.31 m. The results indicate that the CI model offers accurate estimation and demonstrates consistent behavior across all frequencies and distances. Furthermore, compared to the FI model, the CI model boasts a strong physical foundation and lower computational complexity.**

***Keywords*—60 GHz, capacity, FSS, path loss**

I. Introduction

With a theoretical maximum of 6.5 Gbps, the 60 GHz band is an ideal option for attaining the targeted high-speed data rates. In addition to these advantages, it offers a maximum transmit power of 10 W, a high level of frequency reuse, and significant operational savings [1–3].

As compared to other unlicensed channels, the 60 GHz frequency offers substantially higher data speeds. But it gets worse when things get in the way. that limits its usefulness even further. On the 60 GHz spectrum, for instance, signals can be significantly affected by concrete, glass, walls, and any part of a human body. It follows that, with enough reflectors present, the 60 GHz communication spectrum is better suited to short-range and indoor settings [4].

A slight variation in local rules affects the allocation of the 9 GHz sub-bands within the unlicensed 60 GHz spectrum. According to the rules, there are four 2.16 GHz channels in this spectrum. We selected the 61.5 GHz frequency as the second channel for this investigation due to its frequent use as an unlicensed frequency in various locations and countries [5].

In order to determine the capabilities of the network and the overall data throughputs, it is essential to understand the Path Loss (PL) as a function of distance, as well as its temporal and geographical properties. Only simulations or measurements within the channel can achieve this. In order to understand and investigate the attenuation of signal propagation from Transmitter (TX) to receiver (RX), PL Models (PLMs) are crucial. They also allow for the building of accurate channel models for network simulations, which aid in the design of communication systems. To date, Close-In (CI) and Floating Intercept (FI) PLMs have dominated the market for single-frequency applications. There will be an examination of both of these models in this article [6].

Utilization is the main focus of this study, which suggests a new way to manage the spread of the 60 GHz band in a wireless indoor setting by reflecting the whole spectrum and keeping it within the designated area. In order to strengthen the received signal, this method employs Square Loop (SL) frequency selective services (FSSs) wallpaper, which increases multipath propagation as a result of the variety of signal routes.

Moreover, this study improves 5G standards in the 60 GHz band by studying indoor propagation in detail and utilizing various situations to create a large-scale PL model (PLM). Regardless, in order to build a competent indoor system at this frequency, detailed indoor propagation simulations in the 60 GHz region are required for channel characterization and modeling.

Manuscript received February 18, 2024; revised March 27, 2024, accepted April 13, 2024; published July 22, 2024.

The arrangement of this article is as follows: Section II goes over the Equivalent Circuit Model (ECM) analysis technique and how it is applied to the SL FSS wallpaper. Furthermore, it clarifies PLMs for large-scale and Single Input Single Output (SISO) and Multiple Input Multiple Output (MIMO) systems capacity. Next, Section III examines the simulation results and discussion. It begins with the SL FSS wallpaper, and its transmission (S_{21}) and reflection (S_{11}) coefficients, using both MATLAB and CST Studio Suite. Then, demonstrating investigations of some selected scenarios using 'Wireless InSite'. In addition, it presents PLMs results. Also, it presents the SISO and MIMO capacity enhancement results. Finally, Section IV concludes this paper.

II. System Model

A. SL FSS Wallpaper

The frequency selective response of FSSs, which are planar periodic structures, is based on the interference produced by the periodic arrays of dielectric and conducting materials, and they can be employed as filters for a certain frequency of electromagnetic waves [7–9]. SL, ring, dipole, cross dipole, Jerusalem cross, and tripole are some of the common shapes and geometries seen in FSSs. Every one of these varieties can operate as a band-pass, low-pass, high-pass, or band stop filter [9].

Most of the previous studies showed that the SL FSS has the best performance and stability to work within the angular sensitivity, cross polarization Transverse Electric (TE) or Transverse Magnetic (TM) modes, and small band separation [10]. Therefore, we have selected the SL FSS shape for our study.

In order to test SL FSS, ECM has been considered a simple method. The first usage of the ECM technique, first applied to frequency selective circuits, was by Anderson [11]. The advantage of ECM is that it can quickly characterize the FSS response with varying element dimensions. However, ECM can only predict the performance of basic shapes such as SL FSS [12].

The frequency response in SL FSS is determined by the element dimensions (p, d, s, g), as shown in Fig. 1, where p is the separation period, d is the dimension of the loop, s is the width of the conducting strip, and g is inter-element spacing. These parameters determine the location of the f_r (resonant frequency). The parameter g controls the FSS angular performance [13]. Previous studies have suggested that a bigger SL in size is generally effective at a lower f_r and a smaller g ensures stable f_r with varying incidence angles [14].

The ECM technique implies that the interaction between the incident wave and the FSS is represented as a wave propagating through a transmission line, with shunt lumped circuit impedances. The shunt impedance could be inductive or capacitive, relying on whether the polarization of the incident signal is parallel or perpendicular to the strip. Fig. 2 illustrates the approximation of the two adjacent strips as a single strip, width (w) equal to ($2s$) [15]. The normalized shunt inductive reactance expression of the inductive strip was given as in [16]:

$$X_{TE} = \frac{\omega_o L}{Z_o} = \frac{p\,cos(\theta)}{\lambda}\left[ln\left(csc\left(\frac{\pi w}{2p}\right)\right) + G(p,w,\lambda,\theta)\right] \quad (1a)$$

$$X_{TM} = \frac{p\,sec\,\emptyset}{\lambda}\left[ln\left(csc\left(\frac{\pi w}{2p}\right)\right) + G(p,w,\lambda,\emptyset)\right] \quad (1b)$$

The normalized shunt capacitive susceptance expression was given as in [12] by Lee:

$$B_{TE} = \frac{\omega_o C}{Y_o} = \frac{4p\,sec(\theta)}{\lambda}\left[ln\left(csc\left(\frac{\pi g}{2p}\right)\right) + G(p,g,\lambda,\theta)\right]\varepsilon_{eff} \quad (2a)$$

$$B_{TM} = 4F(p,g,\lambda) = \frac{4p\,cos\,\phi}{\lambda}\left[ln\left(csc\left(\frac{\pi g}{2p}\right)\right) + G(p,g,\lambda,\emptyset)\right]\varepsilon_{eff} \quad (2b)$$

where G is the correction term:

$$G\left(p,w,\lambda,\frac{\theta}{\emptyset}\right) = \frac{0.5(1-\beta^2)^2\left[\left(1-\frac{\beta^2}{4}\right)(A_{1+}+A_{1-})\right]+4\beta^2A_{1+}A_{1-}}{\left(1-\frac{\beta^2}{4}\right)+\beta^2\left(1+\frac{\beta^2}{2}-\frac{\beta^4}{8}\right)(A_{1+}+A_{1-})+2\beta^6A_{1+}A_{1-}} \quad (3a)$$

$$G\left(p,g,\lambda,\frac{\theta}{\emptyset}\right) = \frac{0.5(1-\beta^2)^2\left[\left(1-\frac{\beta^2}{4}\right)(A_{1+}+A_{1-})\right]+4\beta^2A_{1+}A_{1-}}{\left(1-\frac{\beta^2}{4}\right)+\beta^2\left(1+\frac{\beta^2}{2}-\frac{\beta^4}{8}\right)(A_{1+}+A_{1-})+2\beta^6A_{1+}A_{1-}} \quad (3b)$$

where

$$A_{1\pm}^{TE} = \frac{1}{\sqrt{\left(\frac{p\,sin\,\theta}{\lambda}\pm 1\right)^2-\frac{p^2}{\lambda^2}}} - 1 \quad (4a)$$

$$A_{1\pm}^{TM} = \frac{1}{\sqrt{1-\frac{p^2\,cos\,\emptyset}{\lambda^2}}} - 1 \quad (4b)$$

and

$$\beta = sin(0.5\pi w/p) \quad (5a)$$

or

$$\beta = sin\left(\frac{0.5\pi g}{p}\right) \quad (5b)$$

where Z_o =377Ω, θ is the incidence angle, λ is the wavelength in air at operating frequency, w is equal to $2s$ in this calculation, and ε_{eff} is the effective permittivity of the surrounding dielectric substrate that influences the capacitance value.

Equations, which are presented in this section, have shown that the FSS response is a function of SL element dimensions, incidence angles, and the dielectric material that holds and gives support for the FSS. In addition, these equations are valid for $[p(1+sin\theta)<\lambda]$ for TE-wave incidence and $[p(cos\theta)<\lambda]$ for TM-wave incidence for a given range of incidence angle. The equivalent impedance of the SL FSS is given by:

$$Z_{FSS} = j\left(X_L - \frac{1}{B_c}\right) \quad (6)$$

hence, the normalized impedance (Z_n) for the transmission line circuit, as illustrated in Fig. 3, can be determined by:

$$Z_n = \frac{Z_{FSS}}{Z_o} = j\left(\frac{X_L}{Z_o} - \frac{1}{B_c Z_o}\right) = j\left(\frac{X_L}{Z_o} - \frac{Y_o}{B_c}\right) \quad (7)$$

By using the $ABCD$ matrix, the S_{21} and S_{11} coefficients for the SL FSS can be determined. As it is known that an $ABCD$ matrix can represent any given network; based on the $ABCD$ parameters, the S_{21} and S_{11} can be determined [17]. For example, for a T-network as illustrated in Fig. 3, the $ABCD$ matrix is presented by:

$$\begin{bmatrix} A & B \\ C & D \end{bmatrix} = \begin{bmatrix} 1 + \frac{Z_1}{Z_3} & Z_1 + Z_2 + \frac{Z_1 Z_2}{Z_3} \\ \frac{1}{Z_3} & 1 + \frac{Z_2}{Z_3} \end{bmatrix} \quad (8)$$

the scattering S-matrix is defined as:

$$\begin{bmatrix} S_{11} & S_{12} \\ S_{21} & S_{22} \end{bmatrix} = \begin{bmatrix} \frac{A+B-C-D}{\Delta} & \frac{2(AD-BC)}{\Delta} \\ \frac{2}{\Delta} & \frac{-A+B-C+D}{\Delta} \end{bmatrix} \quad (9)$$

where $\Delta = A + B + C + D$. For the SL FSS, $Z_1 = Z_2 = 0$ and $Z_3 = Z_n$ as defined in Eq. (9). Therefore, based on Eqs. (10, 11), the S_{21} and S_{11} for the FSS can be evaluated. Because of symmetry $S_{11} = S_{22}$ and $S_{12} = S_{21}$. The $ABCD$ matrix can be expressed as a function of S_{21} and S_{11} as:

$$S_{21} = \frac{2}{A+B+C+D} = \frac{2}{1+0+\frac{1}{Z_3}+1} = \frac{2}{2+\frac{1}{Z_3}} = \frac{2}{2+Y} = T \quad (10)$$

$$S_{11} = \Gamma = 1 - |T|^2 = 1 - \frac{4}{4 + Y^2} \quad (11)$$

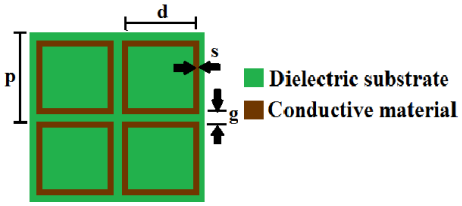

Fig. 1. Array of SL FSS elements.

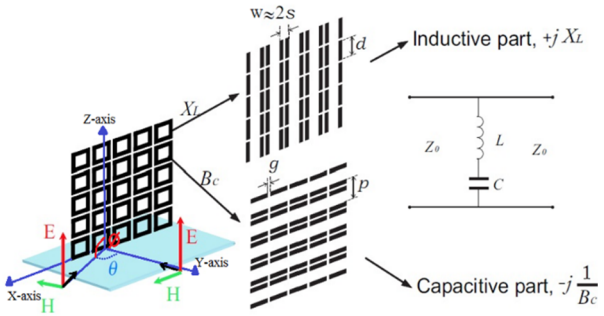

Fig. 2. Inductive and capacitive parts of the SL FSS shape [4].

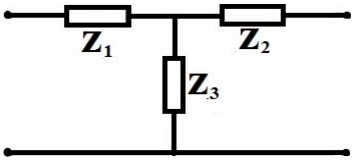

Fig. 3. The $ABCD$ matrix can be used to represent a transmission line.

B. Large-Scale PLMs

In order to construct effective communication systems, large-scale PLMs are essential for estimating the attenuation over distance of propagation signals. A measurement-based PLM gives realistic insight into the propagation properties of a wireless channel [6]. Other forms of large-scale PLMs include deterministic, empirical, and stochastic. This study deals with two varieties of PLMs: CI and FI. According to [18–21], the CI PLM is defined by the path loss exponent (PLE) n:

$$PL^{CI}(f,d)\,[dB] = FSPL(f,d_o) + 10n\log_{10}\left(\frac{d}{d_0}\right) + X_\sigma^{CI} \quad (12)$$

$$FSPL(f,d_o) = 10\log_{10}\left(\frac{4\pi d_o}{\lambda}\right)^2 \quad (13)$$

where λ is the wavelength in m, d_o=1 m, and X_σ^{CI} is a zero mean Gaussian random variable with standard deviation σ^{CI} given by [6]:

$$X_\sigma^{CI} = PL^{CI}[dB] - FSPL(f,d_o)[dB] - 10n\log_{10}(d) = A - nD \quad (14)$$

$$\sigma^{CI} = \sqrt{\sum \frac{X_\sigma^{CI^2}}{N}} = \sqrt{\sum \frac{(A-nD)^2}{N}} \quad (15)$$

where $A = PL^{CI}(f,d)[dB] - FSPL(f,d_o)[dB]$, $D = 10\log_{10}(d)$, and N counts the points at which PL has been measured. A physically based reference distance, d_o, is utilized by the CI PLM, and the mean PLE, denoted as n, shows the rate of growth of PL with distance. One way to determine the FI PLM, which is currently utilized in standardization efforts like the 3rd generation partnership project (3GPP) [22–26]:

$$PL^{FI}(d)[dB] = \alpha + 10\beta\log_{10}d + X_\sigma^{FI} \quad (16)$$

Assume that $B = PL^{FI}(d)\,[dB]$ and the zero mean Gaussian random variable is [6]:

$$X_\sigma^{FI} = B - \alpha - \beta D \quad (17)$$

and the standard deviation σ^{FI} is [6]:

$$\sigma^{FI} = \sqrt{\sum \frac{X_\sigma^{FI^2}}{N}} = \sqrt{\sum \frac{(B-\alpha-\beta D)^2}{N}} \quad (18)$$

according to [6] an α is the floating intercept:

$$\alpha = \frac{\sum D \sum BD - \sum D^2 \sum B}{(\sum D)^2 - N\sum D^2} \quad (19)$$

where β is the line's slope, which is distinct from the PLE, and given by [6]:

$$\beta = \frac{\sum D \sum B - N\sum DB}{(\sum D)^2 - N\sum D^2} \quad (20)$$

where X_σ^{FI} is a log-normal random variable with mean 0 dB and a standard deviation σ^{FI}.

C. SISO and MIMO Systems Capacity

The response to the aforementioned system is assessed by studying the capacity metric. Here is an equation that can be used to calculate the capacity of the SISO system [17]:

$$C_{SISO} = \log_2(1 + SNR) \quad (21)$$

where SNR stands for signal-to-noise ratio. In order to ascertain the capacity, the 2x2 MIMO model's formulation is as follows [17, 27, 28]:

$$C_{MIMO} = \log_2 det\left(I + \frac{SNR}{n} HH^T\right) \quad (22)$$

where the variables det, I, n, H, and H^T are all relevant. Here, det is the determinant, I is the 2×2 identity matrix, n is the number of antennas utilized (2 in this case), H is the channel matrix, and H^T is the channel conjugate-transpose matrix. Using the following formula by [17], we can find H by adding up all the rays that reach each RX antenna:

$$h_{ij} = \sum_{k=1}^{M} \sqrt{P_k} \cdot e^{i(2\pi/\lambda)l_k} \cdot e^{i2\pi f_0 T_k} \quad (23)$$

where M is the number of received rays, P_k is the received power, l_k is the length of the k^{th} ray, f_0 is the carrier frequency, and T_k is the time delay of the k^{th} ray. P_k, l_k, and T_k are obtained from 'Wireless InSite'.

III. Results and Discussion

A. SL FSS (MATLAB)

The proposed design of the SL FSS element's theoretical ECM equations has been solved using MATLAB, where resonance occurs when each half loop acts as a dipole [4, 9]. The basic rule of thumb in designing loop circumference is to make its response approximately equal to the resonant frequency (61.5 GHz). Basic design rules for SL FSS element dimensions are given along with equations for the ECM. Where its dimensions are: p=1.4 mm, s =0.1 mm, d =1.2 mm, g =0.2 mm, and $\varepsilon_{eff} = \frac{\varepsilon_r+1}{2}$=2. For the planned SL FSS at a 0° incidence angle, Fig. 4 shows the S_{21} responses coefficient and Fig. 5 shows the S_{11} responses coefficient.

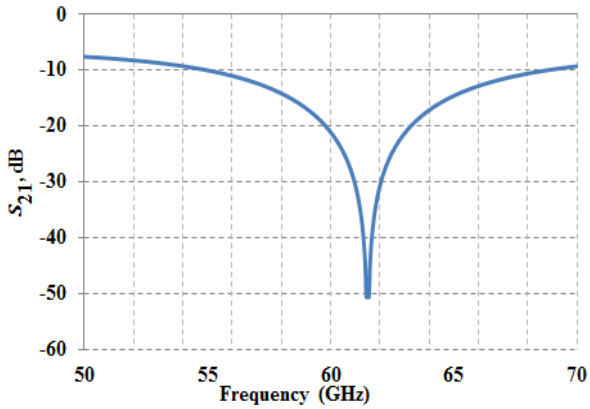

Fig. 4. The reaction of SL FSS wallpaper to frequency transmission, as predicted by ECM equations.

B. SL FSS (CST Studio Suite)

The SL FSS parameters that were designed are tested and analyzed using CST Studio Suite. Finite integration on either a Cartesian or a tetrahedral grid is the analysis method choice, as shown in Fig. 6. Figs. 7 and 8, respectively, display the S_{21} for TE and TM modes for various incidence angles ranging from 0° to 60°. Figs. 9 and 10, respectively, display the S_{11} for the TE and TM modes. The presented coefficients of S_{21} and S_{11} are for frequencies ranging from 50 to 70 GHz.The material utilized for conducting is copper, which has a thickness of 0.07 mm. Arlon AD 300, a dielectric with a relative permittivity of 3, and a thickness of 0.1 mm is used.

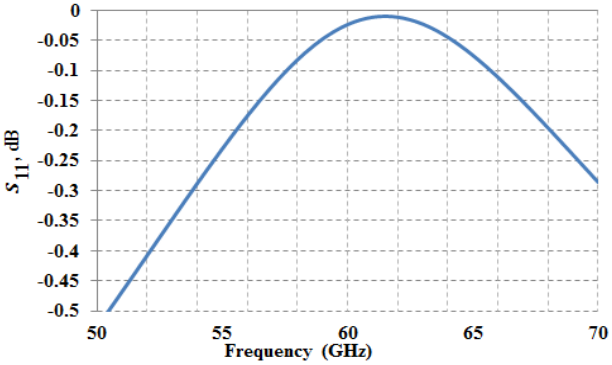

Fig. 5. The reaction of SL FSS wallpaper to frequency reflection, as predicted by ECM equations.

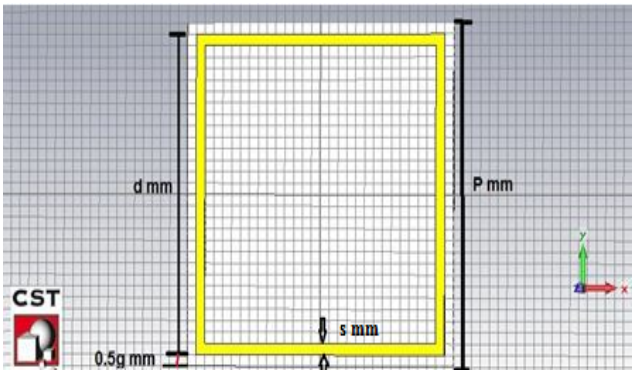

Fig. 6. The SL FSS dimensions, where p = 1.4 mm, g = 0.2 mm, d = 1.2 mm, and s = 0.1 mm.

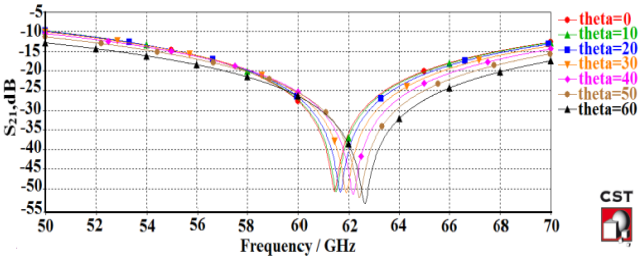

Fig. 7. The S_{21} response coefficient of SL FSS wallpaper for TE-mode.

At the resonant frequency (61.5 GHz), the attenuation value must be more than –25 dB to eliminate the signal, while testing the filter's performance as a band-stop [9]. The S_{21} coefficients for both the TE and TM modes are more than –25 dB, as demonstrated in Figs. 7, 8. As a result, any attempt to enter the target area will result in a dead signal. The SL FSS wallpaper accomplishes its purpose by functioning as an ideal reflector within the region of interest, since the S_{11} coefficients displayed in Figs. 9, 10 are less than –0.05 dB at 61.5 GHz.

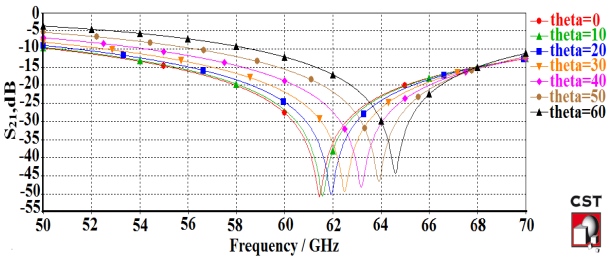

Fig. 8. The S_{21} response coefficient of SL FSS wallpaper for TM-mode.

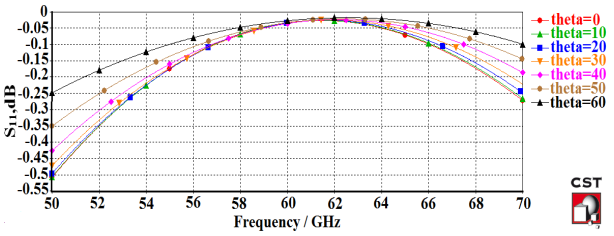

Fig. 9. The S_{11} response coefficient of SL FSS wallpaper for TE-mode.

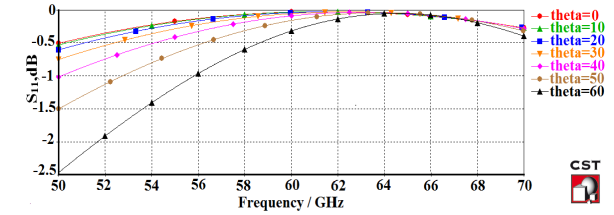

Fig. 10. The S_{11} response coefficient of SL FSS wallpaper for TM-mode.

C. Investigation of Scenarios Using 'Wireless InSite'

In order to assess the received power in various situations inside the desired region, "Wireless InSite" is employed. With the use of 'Wireless InSite,' we were able to extract the SL FSS wallpaper response by exporting the values of the S_{11} and S_{21} coefficients. The analyzed situation took place in a room measuring 15×10 m. The target scenario investigates a MIMO communication system with/without SL FSS wallpaper, while MIMO scenario studies two more sub-scenarios; with/without human bodies.

1) MIMO system scenario

a) MIMO without SL FSS wallpaper

A 2□2 MIMO communication system is used in this scenario for both the TX and the RX's. Both the TX and RX's are assumed to have two antenna elements spaced by λ/2 [7, 29, 30]. The RX are distributed in 20 locations, and each one has an omnidirectional antenna with a sensitivity of -64 dBm and a height of 1.5 m. The TX has a directional antenna with 10 dBm input power, 14 dBi gain, 2.5 m height, and 90° HPBW.

Without human bodies

Exhibited in Figs. 11 and 12, respectively, are the 2D and 3D representations of this situation. Table I presents the electrical parameters of the materials used in this paper [9]. Fig. 12 presents a 3D view of the first scenario, studied without SL FSS wallpaper. Fig. 13 displays the received signal power for each RX site.

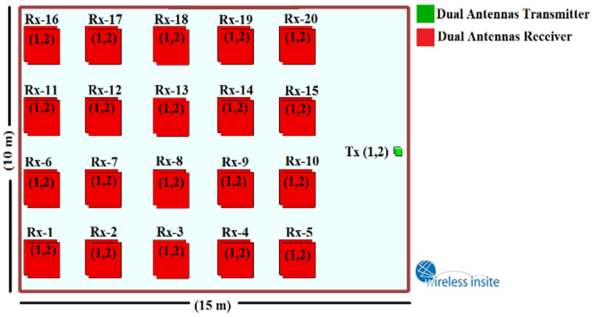

Fig. 11. 2D view for the MIMO scenario.

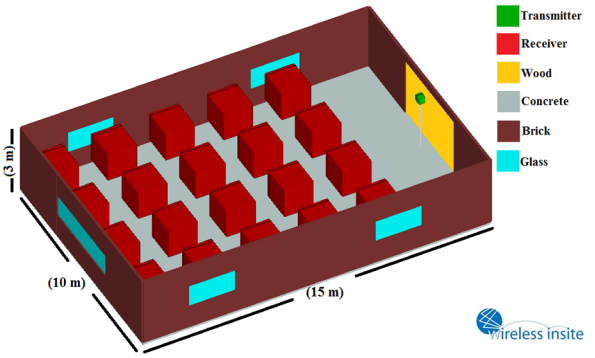

Fig. 12. 3D view for the MIMO scenario without SL FSS wallpaper and human bodies.

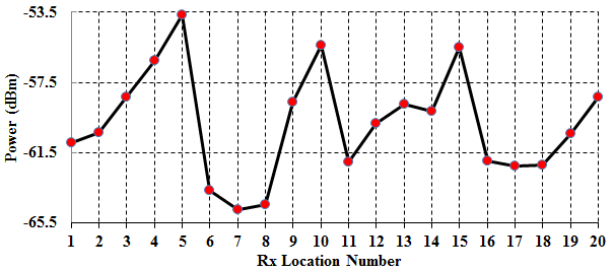

Fig. 13. The received signal power for each RX location number for the MIMO system scenario without SL FSS wallpaper and human bodies.

TABLE I. ELECTRICAL PARAMETERS UTILIZED FOR THE AREA OF INTEREST [9]

Component	Material	Conductivity, σ (S/m)	Relative Electrical Permittivity, ε_r	Thickness (m)
Walls	Brick	0.001	4.44	0.150
Ceiling and Floor	Concrete	0.015	15	0.3
Windows	Glass	0	2.4	0.003
Doors	Wood	0	5	0.03

With human bodies

Both the 2D and 3D representations of this situation are displayed in Figs. 14 and 15, respectively. A random choice of human beings locations are depicted by the black parallelepipeds inside the area of interest. According to Table II, the human body has been modeled inside "Wireless InSite" using the complicated permittivity values of its constituent parts, which include skin, fat, muscle, and pure water, at a resonance frequency of 60 GHz [4]. Fig. 16 shows the received powers at each RX site. Fig. 17 indicates that, on average, human bodies reduce the average received power in the MIMO system by 3 dB.

TABLE II. COMPLEX PERMITTIVITY AT 60 GHZ OF HUMAN BODY COMPONENTS [4]

Human Tissues	ε_c
Skin	$7.98 - j10.91$
Fat	$2.51 - j0.84$
Muscle	$12.85 - j15.74$
Pure Water (20° C)	$11.9 - j19.5$

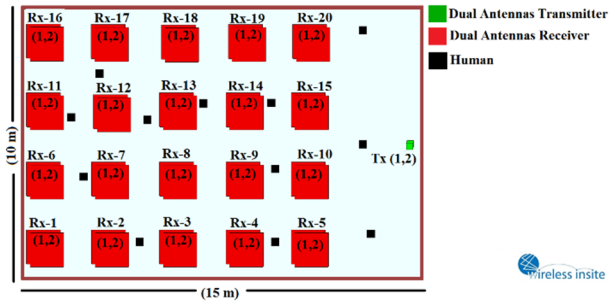

Fig. 14. 2D view for the MIMO scenario without SL FSS, but with a number of human bodies.

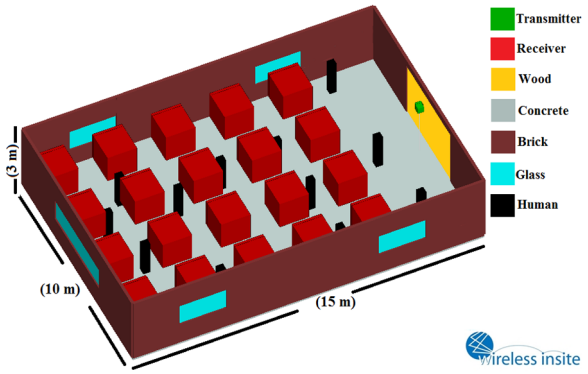

Fig. 15. 3D view for the MIMO scenario without SL FSS wallpaper, but with a number of human bodies.

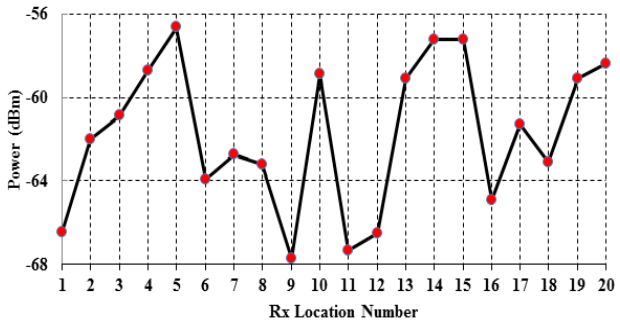

Fig. 16. The received signal power for each RX location number for the MIMO system scenario without SL FSS wallpaper, but with a number of human bodies.

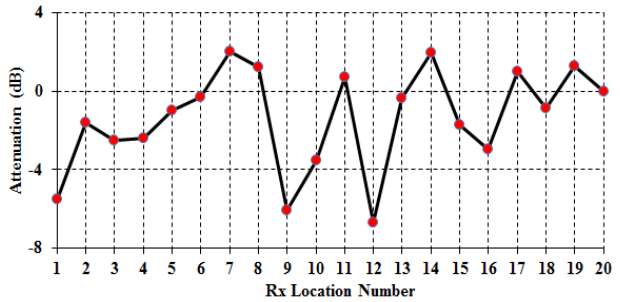

Fig. 17. The received signal power for each RX location number for the MIMO system scenario without SL FSS wallpaper, but with a number of human bodies.

b) *MIMO with SL FSS wallpaper*

Without human bodies

The scenario depicted in Fig. 12 is replicated by employing the technique of attaching SL FSS wallpaper at a distance of λ/10 from the wall [7, 31], as demonstrated in Fig. 18. A representation of the received signal power at each RX site is shown in Fig. 19.

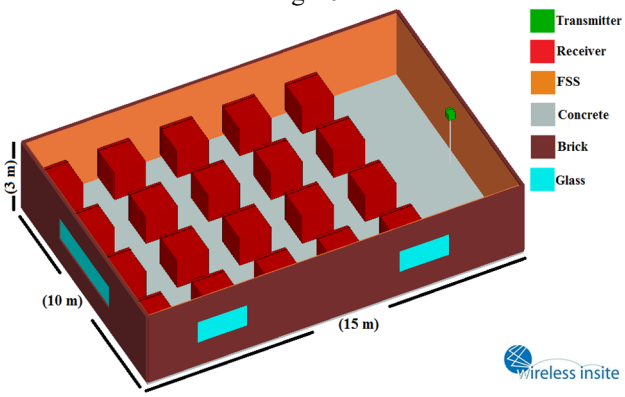

Fig. 18. 3D view for the MIMO scenario with SL FSS wallpaper, but without human bodies.

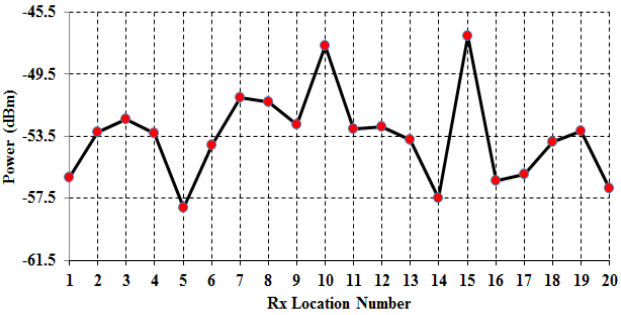

Fig. 19. The received signal power for each RX location number for the MIMO system scenario with SL FSS wallpaper, but without human bodies.

With human bodies

Fig. 20 demonstrates the same situation with several human bodies inserted. At each RX site, the received signal power is displayed in Fig. 21. Fig. 22 shows that when compared to the scenario without human beings, the received power has been lowered by an average of 2 dB in the MIMO system scenario with SL FSS wallpaper and a number of human bodies.

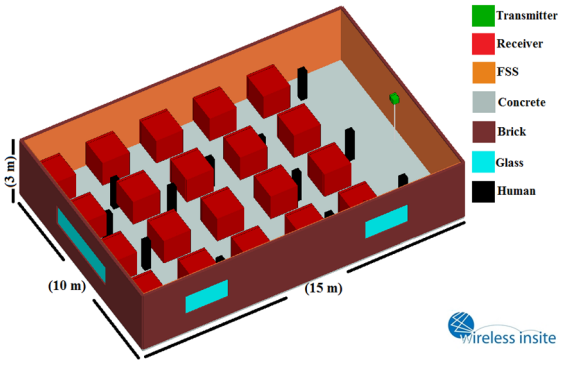

Fig. 20. 3D view for the MIMO scenario with SL FSS wallpaper and a number of human bodies.

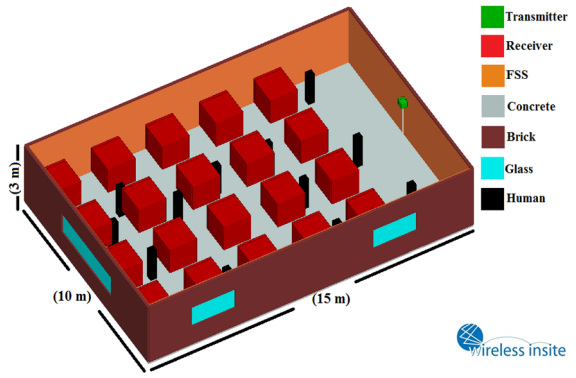

Fig. 21. The received signal power for each RX location number for the MIMO system scenario with SL FSS wallpaper and a number of human bodies.

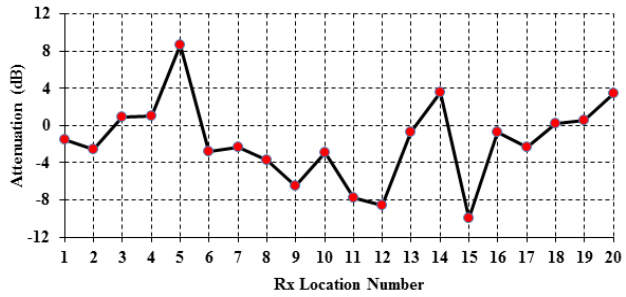

Fig. 22. The achieved attenuation for each Rx location number for MIMO system scenario with SL FSS wallpaper with/without human bodies.

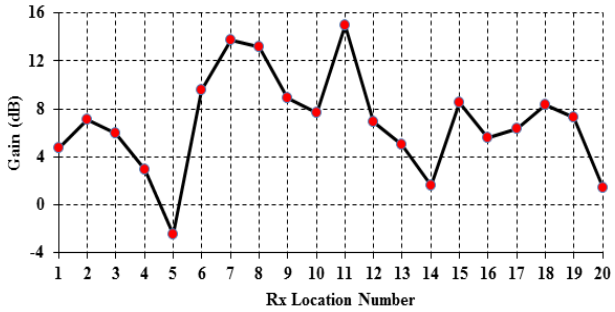

Fig. 23. The gain enhancement for each RX location number between MIMO system scenarios with/without SL FSS wallpaper with human bodies.

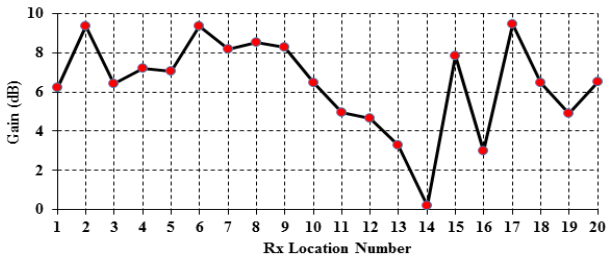

Fig. 24. The gain enhancement for each RX location number between MIMO system scenarios with/without SL FSS wallpaper without human bodies.

Figs. 23 and 24 illustrate the change in the received signal power at each RX site before and after the addition of SL FSS wallpaper, respectively, for the MIMO system scenario with and without human bodies. These statistics show that after applying SL FSS wallpaper, the received power at each RX position has been boosted by an average of 6.87 dB with human bodies and 6.53 dB without. Because the TX's signal experiences additional reflections before reaching the RX, its beam-width has dampened the received power at RX location number 5, as seen in Fig. 23.

D. Large-Scale PLMs

We compare and analyze PL parameters using the two large-scale propagation PLMs given in Section II(B) and the data from indoor simulations for a 60 GHz band. Table III displays the single-frequency CI and FI PLMs parameters at a 60 GHz band for various indoor scenarios. To simplify the comparison and make better use of space, only data captured with vertically-polarized (V-V) TX and RX antennas is included, while omnidirectional antenna data is used for RX.

Table III shows that the physical basis of the CI model allows it to produce intuitive values for the PLM parameters, whereas the parameters in the FI model can at times breach fundamental principles. As a demonstration, consider a scenario where there is no SL FSS wallpaper and the environment is Non-Line-of-Sight (NLOS). In this case, the CI model produces a PLE of 3.39, which is very close to the theoretical free-space NLOS PLE of 4. On the other hand, the FI model produces a PLE of –0.02, indicating that the PL decreases with distance. This is clearly not feasible or reasonable in a passive channel.

The results of the single-frequency PLM parameters highlight the fact that indoor PL is frequency dependent beyond the first meter of FSPL. Table III shows that in the situations without SL FSS wallpaper, the PLEs at 61.5 GHz are greater than in the identical scenarios with SL FSS wallpaper. For 61.5 GHz, the Line-Of-Sight (LOS) PLEs are 1.46 when there is SL FSS wallpaper and 1.7 when there are no people around, suggesting the presence of constructive interference and waveguiding effects in mm-wave LOS interior channels. In addition, the NLOS PLEs are 3.4 and 2.9 at 61.5 GHz for the same circumstances, respectively. This indicates that above the first meter of indoor space, there is a 10 dB increase in attenuation for 61.5 GHz propagating waves, as supplied in Table III. Constructive interference and waveguiding effects in LOS interior channels at mm-wave frequencies are indicated by LOS PLEs of 1.5 and 1.76 at 61.5 GHz, respectively, for scenarios with and without SL FSS wallpaper involving people. Not only that, but the NLOS PLEs 3 and 3.9 at 61.5 GHz are also applicable for the same types of situations. A significant improvement for the NLOS instance was achieved by utilizing the strongest NLOS received power channel from TX-RX (NLOS-Best), resulting in PLE reductions of 2.54 and 2.9, respectively.

In certain instances, the FI model shows less attenuation with respect to log-distance (for example, in the case of humans without SL FSS wallpaper, LOS $\beta = 1$, rather than $n = 1.76$, and NLOS $\beta = -0.02$, rather than $n = 3.39$). On the other hand, when β is negative, the FI model parameters can display unusual, non-physical values. This indicates extremely low loss with distance, lower than in a waveguide, and goes against the principles of basic physics.

Since mm-wave PLM base stations tend to be shorter, housed indoors, or located closer to obstacles, we use d_o=1 m in these cases [23]. The CI model for single-frequencies uses a physically-based 1 m FSPL anchor to simulate free-

space propagation close to the transmitting antenna, allowing for a simpler model with only one parameter. This almost eliminates any decrease in model accuracy. Accordingly, when modeling indoor mm-wave channels, it is more practical to employ the physically sound and simpler CI model that includes a 1 m free space-reference distance term. For co-polarized antennas at TX, 20 LOS, and 122 NLOS readings, scatter plots for CI PLM parameters inside modified indoor environments are shown in Fig. 25.

TABLE III. PARAMETERS FOR THE SINGLE-FREQUENCY CI AND FI PLMS IN A TYPICAL MODIFIED INDOOR SCENARIO

Scenario	Polarization	Frequency (GHz)	Environment	Distance Range (m)	Model	PLE/ β	α [dB]	σ [dB]
SL FSS Wallpaper with Humans	V-V	61.5	LOS	4-14.31	CI	1.5	–	2.68
					FI	0.79	74.8	2.4
			NLOS	4-14.31	CI	3	–	6.4
					FI	0.79	99	3.2
			NLOS-Best	4-14.31	CI	2.54	–	4.2
					FI	0.33	89	1.8
SL FSS Wallpaper without Humans	V-V	61.5	LOS	4-14.31	CI	1.46	-	2.2
					FI	0.76	74	2
			NLOS	4-14.31	CI	2.9	–	6.13
					FI	–0.16	98	2.6
			NLOS-Best	4-14.31	CI	2.5	–	4.2
					FI	0.21	90.5	1.2
Humans without SL FSS Wallpaper	V-V	61.5	LOS	4-14.31	CI	1.76	–	3
					FI	1	75.37	2.74
			NLOS	4-14.31	CI	3.39	–	7.22
					FI	–0.02	101.28	3.87
			NLOS-Best	4-14.31	CI	2.9	–	5.87
					FI	0.15	95	3.34
Without Humans and SL FSS Wallpaper	V-V	61.5	LOS	4-14.31	CI	1.7	–	2
					FI	1.36	74	2
			NLOS	4-14.31	CI	3.4	–	6.88
					FI	0.01	98	3.5
			NLOS-Best	4-14.31	CI	3	–	5.6
					FI	–0.01	90.5	2.24

E. SISO and MIMO Systems Capacity

After SL FSS wallpaper was attached inside the area of interest, Figs. 26 and 27 clearly demonstrate that the capacity for both the SISO and MIMO systems has been boosted. Fig. 26 indicates that, on average, the MIMO system's capacity is 24 bit/s/Hz more than that of the SISO system. According to Fig. 27, the capacity is reduced by an average of 1.25 bit/s/Hz when human bodies are present, and the received signal strength is also affected. In an interior setting, the presence of SL FSS wallpaper increases the strong reflected wave components in each RX site, as seen by an average capacity enhancement of 2.5 bit/s/Hz. The basic premise is that if different multipath components are present at each receiving element, the channel will become more Rayleigh (with a lower K-factor), leading to less correlation and more capacity [9, 17].

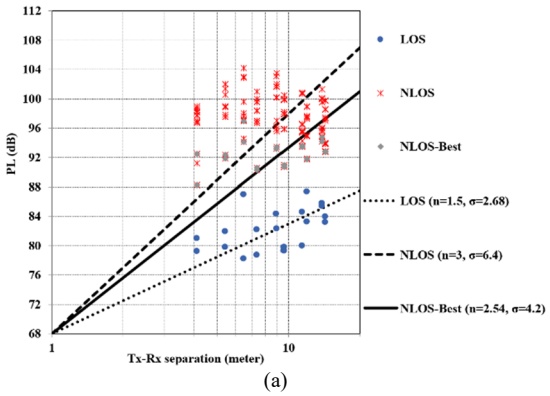

(a)

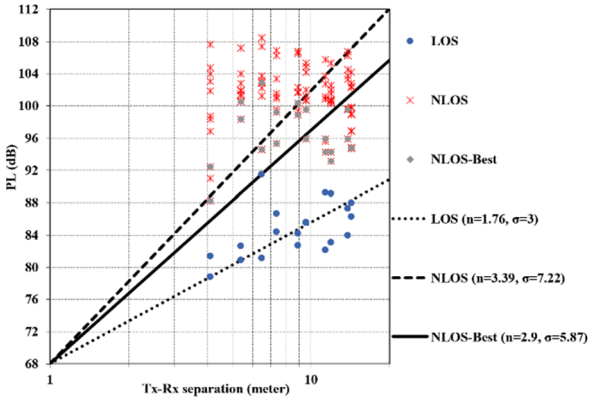

(b)

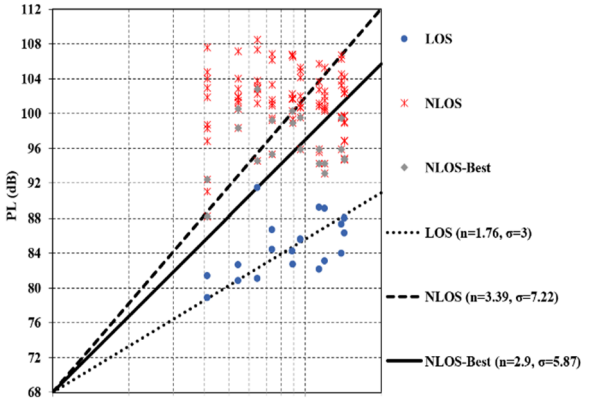

(c)

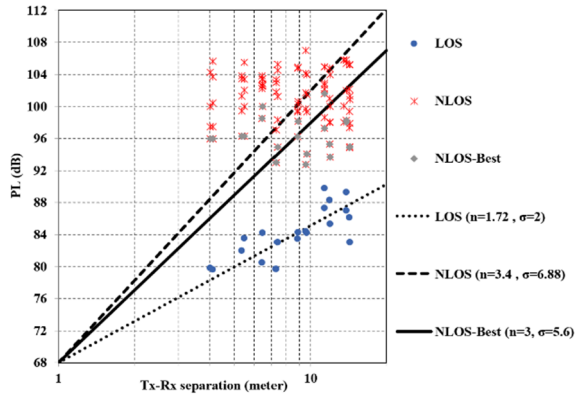

(d)

Fig. 25. Single-frequency (61.5 GHz) CI (d_o= 1 m) PLM parameters scatter plot for TX at a height of 2.5 m, and RX antennas at a height of 1.5 m in an atypically modified indoor office environment for co-polarized antennas, (a) SL FSS wallpaper with humans, (b) SL FSS wallpaper without humans, (c) Humans without SL FSS wallpaper, (d) Without humans and SL FSS wallpaper.

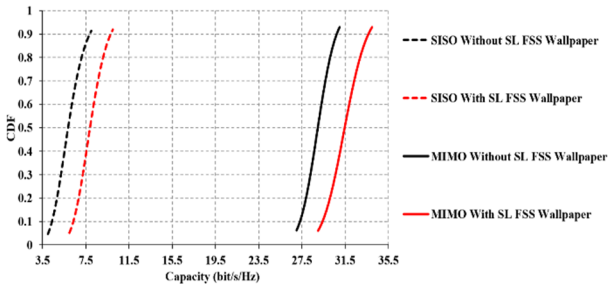

Fig. 26. A Cumulative Distribution Function (CDF) plot showing the comparison between SISO and MIMO systems with and without SL FSS wallpaper for a 60 GHz band.

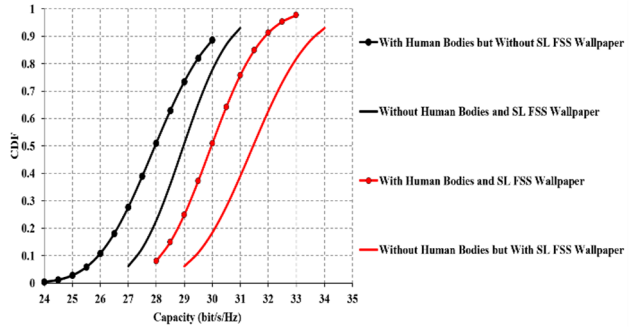

Fig. 27. A CDF plot showing the comparison in the MIMO system between the presence and absence of human bodies, and with/without SL FSS wallpaper for a 60 GHz band.

IV. Conclusion

SL FSS has been chosen to improve the performance of SISO and MIMO systems in indoor 60 GHz wireless networks due to the fact that human bodies and objects can easily obstruct the propagation of 60 GHz. The results demonstrated that SISO improved the received signal power by an average of 6.54 dB, while MIMO improved it by 6.87 dB. On average, capacity was increased by 24 bit/s/Hz when employing a MIMO system. On the other hand, human bodies reduced the capacity by 1.25 bit/s/Hz and weakened the received signal power by 2.5 dB on average. The utilization of SL FSS wallpaper improved the MIMO system's capacity by 2.5 bit/s/Hz on average, demonstrating that the presence of SLFSS wallpaper indoors amplified the strong reflected wave components at each RX point. Also, the results demonstrated that the adjustment caused a minor increase in delay spread, but it was still within the allowed limit for a 60 GHz band, at an average of 7.5 ns. Also given and contrasted in this work are the single-frequency FI and CI PLMs, and mm-wave propagation simulations in altered indoor situations at 61.5 GHz were detailed. The physical basis, simplicity, and robustness over measured frequencies and distance ranges of the CI model made it superior to the FI model (now employed in 3GPP) for modified interior environments, according to single-frequency PL results. A close-in free space reference and standardized measurements around an inherent 1 m free space reference distance physically base the CI model's connection to the transmitter power. Since only one parameter is required, it is simple to implement for different distances (PLE, or n).

Conflict of Interest

The author declares no conflict of interest.

References

[1] M. Alkhawatra and N. Qasem, "Improving and extending indoor connectivity using relay nodes for 60 GHz applications," *International Journal of Advanced Computer Science & Applications*, vol. 7, no. 1, pp. 427–434, 2016. doi: 10.14569/IJACSA.2016.070456.

[2] E. D. Hussein, N. Qasem, M. S. Jameel, M. Ilyas, and O. Bayat, "Performance optimization of microstrip patch antenna using frequency selective surfaces for 60 GHz," in *Proc. 2020 28th Signal Processing and Communications Applications Conference (SIU)*, Gaziantep, Turkey, pp. 1–4, 2020. doi: 10.1109/SIU49456.2020.9302486.

[3] N. Qasem, A. Alamayreh, and J. Rahhal, "Beam steering using OAM waves generated by a concentric circular loop antenna array," *Wireless Networks*, vol. 27, pp. 2431–2440, 2021. doi: 10.1007/s11276-021-02589-z.

[4] N. Qasem, E. A. Aldorgam, and H. Y. Alzou'bi, "Overcoming the influence of human shadowing and obstacles via modified building using frequency selective wallpapers for 60 GHz," *Journal of Communication and Computer*, vol. 13, no. 2, pp. 90–101, 2016. doi: 10.17265/1548-7709/2016.02.004.

[5] H. Azzahhafi, M. E. Yahyaoui, A. E. Moussati, G. E. Zein, and A. G. Armada, "Enhanced 4×4 MIMO RoF architecture for 5G mmWave indoor applications at 60 GHz unlicensed band," *Optics Communications*, vol. 533, p. 129266, 2023. doi: 10.1016/j.optcom.2023.129266.

[6] G. R. Maccartney, T. S. Rappaport, S. Sun, and S. Deng, "Indoor office wideband millimeter-wave propagation measurements and channel models at 28 and 73 GHz for ultra-dense 5G wireless networks," *IEEE Access*, vol. 3, pp. 2388–2424, 2015, doi: 10.1109/ACCESS.2015.2486778.

[7] N. Qasem, "Enhancing the capacity of the Indoor 60 GHz band via modified indoor environments using ring frequency selective surface wallpapers and path loss models," *International Journal of Electrical and Computer Engineering*, vol. 8, no. 5, pp. 3003–3020, 2018.

[8] M. M. M. Sideeq and N. Qasem, "Smart wall based on active frequency selective wallpaper," *ZANCO Journal of Pure and Applied Sciences*, vol. 28, no. 2, pp. 1–6, 2016.

[9] N. Qasem, "Enhancing wireless communication system performance through modified indoor environments," Ph.D. dissertation, Dept. Mechanical, Electrical, and Manufacturing Engineering, Loughborough University, Loughborough, UK, 2014.

[10] T. K. Wu, *Frequency Selective Surface and Grid Array*, Wiley-Interscience, 1995.

[11] I. Anderson, "On the theory of self-resonant grids," *Bell System Technical Journal*, vol. 54, no. 10, pp. 1725–1731, 1975. doi: 10.1002/j.1538-7305. 1975.tb03551. x.

[12] C. K. Lee and R. J. Langley, "Equivalent-circuit models for frequency-selective surfaces at oblique angles of incidence," *Microwaves, Antennas and Propagation,* vol. 132, no. 6, pp. 395–399, 1985. doi: 10.1049/ip-h-2.1985.0070.

[13] C. Mias, C. Tsakonas, and C. Oswald, "An investigation into the feasibility of designing frequency selective windows employing periodic structures," *Radiocommunications Agency Final Rep*, 2001.

[14] B. Munk, *A Frequency Selective Surfaces: Theory and Design*, John Wiley & Sons, 2005.

[15] S. M. A. Hamdy and A. P. Edward, "Current distribution on the elements of a square loop frequency selective surface," *Electronics Letters*, vol. 18, no. 14, pp. 624–626, 1982, doi: 10.1049/el:19820427.

[16] N. Marcuvitz, *Waveguide handbook*, vol. 21, McGraw Hill, 1951.

[17] D. Dawod and N. Qasem, "Enhancing the capacity of MIMO systems via modified building using frequency selective wallpapers," in *Proc. 2015 6th International Conference on Information and Communication Systems (ICICS)*, Amman, Jordan, 2015, pp. 171–176, doi: 10.1109/IACS.2015.7103222.

[18] G. R. MacCartney, S. Deng, and T. S. Rappaport, "Indoor office plan environment and layout-based mmWave path loss models for 28 GHz and 73 GHz," *VTC Spring*, Nanjing, China, 2016, pp. 1–6, doi: 10.1109/VTCSpring.2016.7504287.

[19] M. J. Feuerstein, K. L. Blackard, T. S. Rappaport, S. Y. Seidel, and H. H. Xia, "Path loss, delay spread, and outage models as functions of antenna height for microcellular system design," *IEEE Transactions on Vehicular Technology*, vol. 43, no. 3, pp. 487–498, 1994. doi: 10.1109/25.312809.

[20] M. A. Samad, S. W. Choi, C. S. Kim, and K. Choi, "Wave propagation modeling techniques in tunnel environments: A survey," *IEEE Access*, vol.11, pp. 2199–2225, 2023. doi:10.1109/ACCESS.2022.3233877.

[21] M. A. Samad, D. Y. Choi, H. Son, and K. Choi, "Analysis of centimeter and millimeter-wave path loss at emergency exit," *IEEE Access*, vol. 11, pp. 34217–34226, 2023. doi: 10.1109/ACCESS.2023.3264648.

[22] G. R. MacCartney, M. K. Samimi, and T. S. Rappaport, "Omnidirectional path loss models in New York City at 28 GHz and 73 GHz," in *Proc. 2014 IEEE 25th Annual International Symposium* on *Personal, Indoor, and Mobile Radio Communication (PIMRC)*, Washington, DC, USA, 2014, pp. 227–231. doi: 10.1109/PIMRC.2014.7136165.

[23] T. S. Rappaport, G. R. MacCartney, M. K. Samimi, and S. Sun, "Wideband millimeter-wave propagation measurements and channel models for future wireless communication system design," *IEEE Transactions on Communications*, vol. 63, no. 9, pp. 3029–3056, 2015. doi: 10.1109/TCOMM.2015.2434384.

[24] L. Rubio *et al.*, "Millimeter-wave channel measurements and path loss characterization in a typical indoor office environment," *Electronics*, vol. 12, no. 4, p. 844, 2023. doi: 10.3390/electronics12040844.

[25] A. A. Budalal and M. R. Islam, "Path loss models for outdoor environment—with a focus on rain attenuation impact on short-range millimeter-wave links," *e-Prime-Advances in Electrical Engineering, Electronics and Energy*, vol. 3, p. 100106, 2023. doi: 10.1016/j.prime.2023.100106.

[26] A. Alsalman and N. Qasem, "60 GHz millimeter-wave indoor propagation path loss models," *International Journal of Applied Engineering Research*, vol. 12, no. 22, pp. 12971–12981, 2017.

[27] A. Alamayreh, N. Qasem, and J. S. Rahhal, "General configuration MIMO system with arbitrary OAM," *Electromagnetics*, vol. 40, no. 5, pp. 343–353, 2020, doi: 10.1080/02726343.2020.1780378.

[28] R. Adeogun, "Capacity and error rate analysis of MIMO satellite communication systems in fading scenarios," *International Journal of Electrical and Computer Engineering*, vol. 4, no. 4, pp. 614–622, 2014, doi: 10.48550/arXiv.1408.2023.

[29] H. AlKayyali and N. Qasem, "Convoluted frequency selective surface wallpaper to block the industrial, scientific, and medical radio bands inside buildings," *American Academic & Scholarly Research Journal*, vol. 5, no. 3, pp. 106–112, 2013.

[30] J. X. Sun, M. Z. Chen, and Y. J. Cheng, "Single-PCB fabricated, ultra-wideband, and wide-scanning phased array antenna with vertically integrated resistive frequency selective surface," *IEEE Transactions on Antennas and Propagation,* vol. 72, no. 3, pp. 2411–2422, 2024, doi: 10.1109/TAP.2024.3355209.

[31] N. Qasem, "Enhancing the capacity of SISO & MIMO systems within modified environments using frequency selective surfaces," *Al-Balqa Journal for Research and Studies*, vol. 21, no. 1, pp. 73–88, 2018.